Final Draft

of the original manuscript

Xu, P.; Pyczak, F.; Yan, M.; Limberg, W.; Willumeit-Römer, R.; Ebel, T.:

Tensile toughening of powder-injection-molded β Ti-Nb-Zr biomaterials by adjusting TiC particle distribution from aligned to dispersed pattern.

Tensile toughening of powder-injection-molded β Ti-Nb-Zr biomaterials by adjusting TiC particle distribution from aligned to dispersed pattern

Peng Xu[†, *], Florian Pyczak[‡], Ming Yan[†, §], Wolfgang Limberg[†], Regine Willumeit-Römer[†], Thomas Ebel[†]

[†]Division of Metallic Biomaterials, Institute of Materials Research, Helmholtz-Zentrum Geesthacht, D-21502 Geesthacht, Germany

[‡]Division of Materials Physics, Institute of Materials Research, Helmholtz-Zentrum Geesthacht, D-21502 Geesthacht, Germany

[§]Department of Materials Science and Engineering, Southern University of Science and Technology, 518055 Shenzhen, China

Corresponding author: Peng Xu (P. Xu), E-mail address: peng.xu@hzg.de

Abstract: The powder metallurgically produced β titanium alloys have long been plagued by high impurity contamination. One of them is the carbon contamination of binder-based powder technologies that originates from the sintering atmosphere, the debinding process and the starting powders. In general, a normal carbon residual of binder-based powder technologies is capable of incurring the formation of aligned TiC_x particles along prior β grain boundaries (GB-TiC_x) in most classes of β titanium. Premature intergranular fracture of materials invariably ensues during plastic deformation, which hinders their commercialization in structural applications. A novel toughening strategy by regulating TiC_x precipitation evolution and resultantly adjusting particle distribution is suggested. In this study, biotolerant metastable β Ti-Nb-Zr alloys containing 0.05 wt.% standard carbon residual and consequently 0.5 vol.% *in situ* synthesized TiC_x particles were fabricated via powder injection molding. Synchrotron radiation identified that two separate TiC_x precipitation-type reactions occurred at β phase region and α/β region. In a narrow temperature range between these two precipitation reactions, dissolution of carbides is observed just below α/β transus. Yttrium addition can postpone TiC_x precipitation. On the basis of those mechanisms, adjusting TiC_x particle distribution is proposed for the first time, specifically a combination of yttrium addition (Y) and carbide spheroidization reprecipitation annealing (CSRA). As a result, aligned GB-TiC_x particles were adjusted to dispersed intragranular TiC_x particles. An apparent toughening effect (≈113% increment reaching $\varepsilon_f = 8.3\%$) was achieved after TiC_x redistribution, while non-optimally aligned TiC_x pattern seriously limited tensile toughness of materials by two negative crack propagation modes. Here, the mechanisms of TiC_x redistribution behavior and its toughening are elucidated systematically.

Key words: Powder injection molding, Titanium alloys, Carbides, Particle distribution, Tensile testing, Toughness

Highlights

- A novel sintering pathway adjusting TiC_x particle distribution is first proposed.

- Aligned GB-TiC_x particles are adjusted to dispersed intragranular TiC_x particles.

- The TiC_x redistribution methods effectively toughen PIM β Ti-Nb-Zr biomaterials.

- The mechanisms of TiC_x redistribution behavior and its toughening are elucidated.
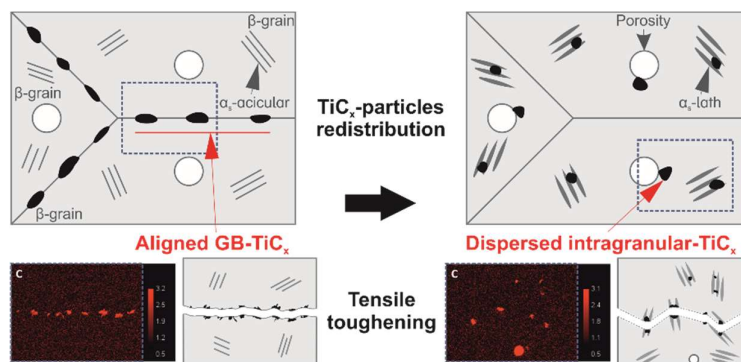
1. Introduction

Metastable β Ti-Nb-Zr alloys, as important classes of titanium alloys that possess inherently superior toughness, i.e. damage tolerance or crack resistance for high plastic strain and cyclic stress, are promising engineering materials in a number of critical structural applications [1-3]. Especially, for biotolerant orthopedic applications, recent concerns to stress-shielding effects, toxic ion release and mechanical fracture also capitalize on the low stiffness, biocompatibility and high mechanical performance of β titanium alloys [4, 5]. They are able to provide, theoretically, an attainable elastic modulus similar to cortical bone (<30 GPa) [6]. Titanium, niobium and zirconium elements have been verified to exhibit minimal cytotoxicity and mutagenicity in transition metals via diverse *in vitro* and *in vivo* evaluations, which display satisfactory properties in regard to biocompatibility and osteogenesis [7-14]. Ti-Nb-Zr-based biomaterials concurrently have manifested self-tunable Young's modulus, good removability and super-elastic performance in recent research [15-17], which is likely endorsed as a new concept for metallic biomaterials in the future. Powder injection molding (PIM) has remarkable industrial application potential and technical advantages to fabricate orthopedic implants, comprised of mass production, high-performance, sophisticated shape and cost-savings [18-20]. Unfortunately, most β titanium alloys fabricated via powder metallurgy technologies (incl. conventional sintering and PIM) have long suffered from embrittlement induced by carbon contamination. Typical contamination sources are generally the starting powder and the sintering furnace atmosphere [21, 22]. Since, binder-based powder metallurgy technologies, such as powder injection molding and binder jetting, utilize polymeric binder; extra carbon uptake commonly takes place during the debinding process, where improper removal of residuals after pyrolysis of polymers often occurs [23, 24].

Carbon with a rather large atomic radius (≈70 pm) has low solubility in the interstitial vacancies of the Ti-lattice, unlike oxygen (≈60 pm) which is highly soluble [25]. Furthermore, the tetrahedral vacancy with $r_{void}/r_{atom} = 0.291$ in the β-Ti body-centered cubic lattice is ≈30% smaller than the octahedral vacancy with $r_{void}/r_{atom} = 0.414$ in the α-Ti hexagonal closed packed lattice, which both are the largest vacancies in respective Ti-lattices [26-29]. The total solubility of carbon thus could be significantly reduced under a high concentration of β-stabilizers. In general, titanium-carbides (TiC_x) consequently precipitate along grain boundaries (GB), i.e. in the form of GB-TiC_x, when carbon concentration exceeds the solubility limit in the Ti-matrix. This low solubility limit is a dominant factor of the high susceptibility of β titanium alloys for embrittlement induced by carbon contamination. It has been widely recognized that GB-TiC_x second-phase particles effect brittle and premature intergranular fracture of powder metallurgically processed β-Ti alloys [24, 30-34]. Such materials exhibiting rather low toughness to strain ratios are not an option for critical structural application, where catastrophic damage is completely unacceptable. Therefore, commercializing them has been severely obstructed until now.

Previous work basically has focused on the characterization of the atomic-scale lattice configuration of TiC_x. Researches demonstrated that TiC_x exists as a stoichiometric composition with diverse carbon contents under various conditions [33, 35-38]. Goretzki et al. [39], claimed that carbon atoms occupy ordered positions of $TiC_{0.5}$, which is a supercell with a twofold lattice constant of the subcell. It also was pointed out that a lower C/Ti atomic ratio (viz. x in TiC_x) can weaken atomic bonding strength (viz. Ti-Ti covalent bonds) in TiC_x to further reduce strength and hardness of TiC_x [40]. A face-centered cubic structure of GB-$TiC_{0.5}$ and its platelet shape in β titanium alloys was revealed and reconstructed by Yan et al. [33]. A few researchers have addressed a metallurgical solution to the premature fracture induced by

GB-TiC$_x$, through technical precaution against TiC$_x$ formation and carbon contamination [24]. Water quenching and high-concentration alloying were indicated as effective to reduce the amount of TiC$_x$ precipitation [32]. To use high-purity original powder, extremely high-purity argon flow in thermal debinding [23] and to run a thorough cleaning program for debinding-sintering furnace (e.g. hydrogen charging burn-out/burn-off) are able to mitigate carbon uptake. However, they may not be completely successful; these methods are typically cost-consuming and technically difficult to perform, or occasionally sacrifice certain mechanical properties.

Instead, a practical alternative that is much more feasible is to accept the existence of TiC$_x$ and distribute the particles not at the grain boundaries but in the grain interior by optimized processing. A small quantity of intragranular TiC$_x$ in β-Ti alloys was also observed in some studies [31, 37, 41, 42]. Optimizing the distribution of second-phase particles, e.g. adjusting aligned GB-TiC$_x$ to dispersed intragranular TiC$_x$, was advised to likely enhance toughness [43, 44]. Lately, Lefebvre et al. [45] observed a positive effect from amorphous graphite addition on sintering densification, strength and elongation of PM CP-Ti and Ti-6Al-4V. All these parameters were prominently improved due to even particle distribution combined with refinement mechanism. Nevertheless, there are only a few studies with respect to adjusting particle distribution, like TiB/Al$_2$O$_3$ second-phase via thermomechanical processing [46, 47], which is not appropriate to low-cost near-net-shape powder technologies. Thus, adjusting TiC$_x$ particles distribution requires more investigations.

In this paper, we explore TiC$_x$ redistribution methods via generating dispersed intragranular TiC$_x$ to replace aligned GB-TiC$_x$ in powder metallurgical β Ti-Nb-Zr alloys. The mechanisms of the TiC$_x$ redistribution induced by yttrium (Y) and carbide spheroidization reprecipitation annealing (CSRA) on TiC$_x$ precipitation are systematically investigated. Specifically, Y works

as a "moderator" that reduces the mean diffusion rate of carbon atoms by lowering the starting temperature of TiC_x precipitation. On the other hand, CSRA can offer plenty of time to break Ti-C bonds and lead originally acicular α-phases to form α-laths. Due to these α-laths providing a great number of effective lattice-vacancies, carbon atoms can diffuse and dissolve into these α-laths, and α-laths keep carbon in dissolution until rather low temperature when TiC_x then precipitates near these α-laths or their bundles. The aligned-agglomerated GB-TiC_x particles are adjusted to evenly-dispersed intragranular TiC_x, thereby toughening PIM-processed Ti-Nb-Zr alloys (PIM-TZN) by mitigating negative crack propagation modes. Furthermore, the effect of different TiC_x particle distribution patterns on tensile toughness is elucidated. This paper aims to propose a better solution for the GB-TiC_x-induced embrittlement of PM β-Ti alloys. Replacing rigorous technical precautions against carbon contamination and TiC_x formation by proper adjustment of TiC_x phases spatial distribution is an incentive for ongoing research.

2. Experimental

2.1. Materials preparation:

Samples from metastable β titanium alloys including Ti-10Zr-20Nb, Ti-10Zr-20Nb-0.1Y and Ti-10Zr-18Nb-0.1Y (wt.%) were fabricated by powder injection molding as described in the following. We use the abbreviations TZN20, TZN20-Y and TZN18-Y respectively throughout this article. Commercially-available pure Ti powder (ASTM Gr.1, <45µm, spherical; TLS Technik, Bitterfeld, Germany), Ti-42Nb master-alloyed powder (<63µm, spherical; H.C. Starck, Goslar, Germany [48]), elemental Zr powder (<45µm, irregular; abcr GmbH, Karlsruhe, Germany) and elemental Y powder (<45µm, irregular; Edgetech Industries, Miramar, USA) were used as starting materials. The composition of the alloys was defined by blending these metallic powders in the corresponding amounts. Ti-42Nb master powder was selected to support homogeneous sintering compared to using purely elemental powders. Additionally, according to the literature [49-51] yttrium and its oxide form (yttria, Y_2O_3) are moderately biocompatible and beneficial for maintaining the homeostatic equilibrium of human beings.

The metallic powders were blended with a polymeric binder system consisting of paraffin wax, polyethylene-co-vinyl acetate and stearic acid. A mixture that comprised 65 vol.% metallic powder and 35 vol.% binder was blended in a kneader (Femix Misch- und Knettechnik GmbH, Waiblingen, Germany) for 4 h at 120 °C under controlled argon atmosphere ($H_2O < 1$ ppm, $O_2 < 1$ ppm). The feedstock for subsequent injection molding was finally acquired after granulating in a crushing mill (Wanner Technik, Wertheim, Germany). The green parts of tensile specimens ("dog bone" geometry, ISO 2740 standard) were injection molded under maximum pressure of 1300 bar via a powder injection machine (Arburg 320S, Lossburg, Germany). In the solvent debinding, the green parts were immersed under hexane (VWR CHEMICALS, Radnor, USA) flow in a commercial debinding device (LÖMI LRA/EBA-50,

Grossostheim, Germany) at 40 °C for 15 h to remove the paraffin wax. Programs including thermal debinding, conventional-sintering cycle and newly-designed extra sintering cycle, i.e. carbide spheroidization reprecipitation annealing (CSRA), were run in a tungsten heater high-vacuum furnace (XERION XVAC 1600, Freiberg, Germany). Specimens were on sintering support of Y_2O_3 layer and protected in shield packs of molybdenum from atmospheric contamination. Thermal debinding was performed with a heating rate of 2 K/min to 600 °C maximum temperature under slight argon flow (purity 99.996%, Linde AG, Munich, Germany) at 5 mbar pressure. As-sintered parts of TZN20, TZN20-Y and TZN18-Y were obtained from a conventional-sintering cycle (1500 °C/4 h under 10^{-4} Pa vacuum, 5K/min heating rate and 10 K/min cooling rate). Such a controlled cooling rate is beneficial to near-equilibrium phase transition and to avoid overgrowth of β grains. The novel CSRA (800 °C/1 h under vacuum, 10K/min heating rate and 2 K/min cooling rate, both thermal profiles are given in the online Supplementary Material for this paper) was performed subsequently on some of the as-sintered parts, which are referred to as: TZN20-CSRA, TZN20-Y&CSRA and TZN18-Y&CSRA, respectively. To ensure comparable carbon uptakes for all specimens, the CSRA program was conducted separately from the sintering cycle.

Binderless pressed and sintered samples (Ø 8 mm × height ≈6 mm) were molded by using a press force of 2.5 kN via a hydraulic press (Enerpac, Menomonee Falls, USA). The utilized powders were exactly the same as above-mentioned PIM-TZN alloys. These cylindrical samples were consolidated via running the conventional sintering program as described before. A vacuum burn-out program, for cleaning the furnace, was always carried out prior to every sintering cycle.

2.2. Materials tests and characterization:

Uniaxial tensile tests were conducted on a servo-hydraulic structural test machine (RM-100, Schenck-Trebel, Deer Park, USA). This machine is modernized with a Zwick DUPS electronic testing system and equipped with a 100 kN load cell and a noncontact laser extensometer (WS 160, Fiedler Optoelektronik GmbH, Lützen, Germany). Tensile properties were determined for three "dog bone" PIM-parts under strict quality control at a strain rate of 0.5 mm/min at ambient temperature.

The concentrations of carbon, oxygen and nitrogen were determined of: i) starting powders, ii) pressed and sintered parts and iii) PIM-processed parts (incl. as-sintered and CSRAed) for unveiling impurity levels and the sources of contamination. In brief, six ultrasonic-cleaned samples corresponding to each state were measured with analysis devices (LECO CS-444 and TC-436AR, Saint Joseph, USA). Porosities of PIM-TZN were calculated from results of relative density measurements that were determined with an electronic balance (Sartorius AG, Göttingen, Germany) by Archimedes' principle outlined in ASTM B962.

The metallographic samples were cut from MIM-processed tensile specimens before and after fracture by tensile tests. They were ground with SiC abrasive papers (Schmitz-Metallographie, Herzogenrath, Germany), polished with neutral OPS solution (Cloeren Technology, Wegberg, Germany) by a TegraPol-35 grinding and polishing machine (Struers GmbH, Willich, Germany), then ultrasonically cleaned in pure ethanol (Merck KGaA, Darmstadt, Germany). Optical microscope (Olympus PMG3, Tokyo, Japan) and scanning electron microscope (Tescan Vega3 SB, Brno, Czech) equipped with energy-dispersive spectroscopy (EDX) were used for microstructural characterization, fractographic study and compositional analyses to preliminarily determine the consistency of chemical composition of two kinds of TiC_x. Average prior β grain size determined for three images of etched samples

were measured by Olympus Soft Imaging Solutions pro. The volume fraction of TiC_x second-phase particles was determined from three 200x optical pictures and averaged by using ImageJ analysis software. The mathematical conversion of the elemental weight percentages from the mapping data was carried out by Iridium Ultra software. Electron backscatter diffraction (EBSD) (Zeiss Ultra 55, Carl Zeiss AG, Germany) was applied to verify the location of TiC_x precipitates. An area of 150×300 μm^2 was scanned at 15 kV for 22 h for PIM-TZN20 series.

2.3. In situ high energy X-ray diffraction (synchrotron):

In order to investigate the evolution of precipitation of TiC_x during cooling, *in situ* high-energy X-ray diffraction experiments were performed at the HEMS beam line run by Helmholtz-Zentrum Geesthacht at the PETRA III of Deutsches Elektronen-Synchrotron (DESY) in Hamburg. The X-ray beam had a cross-section of 5×5 mm^2 and photon energy of 87.1 keV corresponding to a wavelength of 0.14235 Å. The cylindrical specimens (Ø ≈4.5 mm × height 10 mm) of PIM-processed TZN20 and TZN20-Y were measured in transmission. The diffractograms of Debye-Scherrer diffraction rings with an exposure time of 0.5 s were recorded every 15 s using a PerkinElmer XRD 1622 flat panel detector (2048 × 2048 pixels, pixel size = 200×200 μm^2). The specimens in a vacuum were heated up to 1000 °C and held for 15 min until all carbides were dissolved and no carbide peak was detectable anymore. Subsequently, these specimens were cooled to 600 °C by 2 K/min, and afterwards quenched to 25 °C by fast cooling. As a measure for the precipitation percentage of carbides, the reflection intensities of the carbide peak of the (220) reflection was taken at different temperatures and compared to the intensity of that peak at ambient temperature. However, the strong peak positions of the (111) and (200) reflections from carbides were not taken to quantify the carbide fraction, due to surrounding background intensity from α-Ti and β-Ti peaks. The series of two-dimensional diffraction data obtained from the flat panel detector were converted into series of one-

dimensional diffraction patterns (2θ versus intensity) by analysis software (Fit2D, Andy Hammerley). The amount of precipitation of carbides at a certain temperature was determined by the integral of their (220) diffraction peak (the area underneath the curve). The critical values that can represent the evolution trend of TiC_x precipitation in relation to temperature are given.

3. Results

3.1. Contamination sources of PIM technology:

The results on basic impurities of as-sintered and CSRAed PIM-TZN alloys are listed in Table 1. The carbon contents were essentially the same, varying over a small range near 0.05 wt.%, which is considered as the standard amount of carbon residual for PIM. Residual amounts of carbon derived from several sintering cycles exhibit a basically repeatable level. Also, the minor differences of their oxygen or nitrogen concentrations are negligible. There seems to be no significant influence of the extra CSRA exposure and the slightly varying alloy compositions on interstitial contents. Moreover, the volume fractions of TiC_x in TZN20 series were essentially constant at about 0.5 vol.% regardless of CSRA or Y, whereas the cases in TZN18 series just show almost half of the amount in comparison of TZN20 series, due to the lower Nb content in charge of carbon solubility.

Comparing the results on carbon contents in Table 2 indicates to what extent starting powders, debinding process and sintering atmosphere contributed to carbon contamination in the final PIM-components. Unexpectedly, the final carbon residuals in binderless pressed and sintered parts were higher than in the binder-based PIM parts. Oxygen residue was in line with this tendency as well (≈ 0.32 wt.%, extra 0.05 wt.% oxygen). It may imply that improper thermal pyrolysis of polymers in debinding process did not contribute too strongly to carbon contamination, but sintering atmosphere plays the critical role. Previously, it was reported that sintering (incl. atmosphere and support) contributed to the majority of oxygen contamination in Ti-6Al-4V (<45 µm-sized pre-alloyed powder) [22]. Although a burn-out step is carried out prior to sintering cycle of PIM, ashes of organic materials may still remain in complex-configuration debinding-sintering furnaces. In this case, it was difficult for the pressed and sintered parts, obtained by lower pressure molding, to attain a powder loading as high as the

PIM technology. Consequently, comparatively low densification (≈90%) and large external surface of pressed and sintered parts lead to a higher possibility of atmospheric exposure and accordingly contamination than PIM-parts. Ebel et al. [52], advised that placing oxygen traps like titanium sponge with high surface area is helpful for reducing the contamination uptake from sintering atmosphere. It can be expected that the same means work to trap carbon.

3.2. Analyses of particle characteristics of TiC$_x$:

3.2.1. OM

Figure 1 shows the optical micrographs of all alloys in as-PIMed and PIM+CSRAed state. Platelet-shaped particles with rather large size are distributed in an aligned mode in conventional-sintered TZN20 (see Figure 1(a)). This distributional feature is practically the same as in many previous reports [31, 32, 37, 41, 42, 53, 54]. By contrast, the particles in TZN20&CSRA and TZN20-Y indicate a neutral distribution mode; a few aligned particles were visible in some cases, but not as many as in TZN20, as marked by arrows in Figure 1(b)(c). Whereas, it can be observed that rather tiny dispersoids are evenly-dispersed throughout TZN20-Y&CSRA (Figure 1(d)). The uniform particle distribution of TZN18-Y(&CSRA) alloys is basically the same as in TZN20-Y&CSRA, but the number of particles is obviously lower (Figure 1(e)(f)). Because the particle distribution of TZN18 series is not significantly affected by CSRA, they were specifically designed and introduced into this study as a reference group for discussion in section 4.3. Besides, there was a slightly higher porosity in the alloys with yttrium addition, which may be due to the fact that large yttrium and yttria powder particles degrade sinterability [55].

3.2.2. EDS preliminarily chemical analysis

As described above, particle distributions in TZN20 and TZN20-Y&CSRA were extremely different, specifically aligned-agglomerated and evenly-dispersed patterns, respectively. In this report, we confine the preliminary characterization of the particles on their stoichiometry and morphology, reporting first about stoichiometry in this section. Investigations of the crystalline configuration of TiC_x have been extensively performed by other authors in the past decades.

The average values ± variance of chemical elements in aligned and dispersed particles determined for 10 sites of each type are summarized in Table 3. Taking the variances into account, the minor differences between aligned and dispersed particles can be neglected. Therefore, the particles were assumed to be of the same structure and chemistry. A simple reasonability check for the results is deduced in the following. A value for the carbon concentration in present TiC_x was estimated on the basis of the densities (ρ_{TZN20}=4.95 g/cm^3, ρ_{TiC}=4.93 g/cm^3), and we assumed a premise that all carbon atoms in the particles were bound in TiC_x form (0.05 wt.% C formed 0.5 vol.% TiC_x), i.e. no carbon was dissolved in Ti-matrix. An upper limit of carbon concentration of TiC_x of 32 at.% (i.e. x < 0.48 in TiC_x) was calculated. Apparently not all carbon atoms are contained within precipitates, accordingly the concentration is supposed to be lower than 32 at.%. The measured values of approximately 16 at.% are thus in a reasonable range, i.e. about half of carbon atoms are in the Ti-matrix. It means that a carbon solubility limit of ≈0.025 wt.% is estimated in TZN20 series. This limit was thought also to be in fairly good agreement with the predicted maximum carbon limit of 0.023 wt.% in Ti-16Nb [33], of which carbon limit may be more or less similar with TZN20 (Ti-10Zr-20Nb), due to Zr increasing carbon solubility [32] but a higher Nb content acting in the opposite direction. In addition, a similar initial precipitation temperature of TiC_x in Ti-16Nb implies essentially the same of lattice constant in charge of the solubility limit.

Figure 2 displays BSE and mapping images of local areas surrounding the particles; the weight percentages of elements were expressed by color intensity. Interestingly, TiC_x contained strikingly more Zr and less Nb than the Ti-matrix. A possible explanation is given here; Zr atoms expand β Ti-lattice constants [32], while Nb decreases it [53]. Furthermore, the lattice space of fcc-TiC_x supercells enlarges with increasing number of carbon atoms [56]. It is reasonable to suppose that the TiC_x superlattice tends to capture Zr atoms that are diffusing near TiC_x to substitute Ti atoms (or likely Nb) in order to achieve a localized lowest lattice deformation energy. This substitution associated with the fact that Zr also is a strong carbide former in some cases is responsible for the observed hybrid TiC_x ($Ti_aZr_bC_xO_c$).

3.2.3. EBSD

The TiC_x precipitating location, i.e. either GB-TiC_x or intragranular TiC_x particles, can be identified from EBSD (Figure 3). The majority of TiC_x particles distributed rigorously in alignment along some prior β grain boundaries, which are GB-TiC_x, as displayed in Figure 3(a); this is the aligned-agglomerated distribution pattern and widely recognized as TiC_x particles in powder metallurgically sintered β titanium alloys. Figures 3(b)(c) seem to represent a sort of transition, specifically almost half of the TiC_x particles remained inside the β-grains, the rest is located at grain boundaries. However, the inspection of Figure 3(d) indicates that a substantial amount of TiC_x dispersoids is embedded in the interior of prior grains (intragranular TiC_x) in a rather uniform mode; barely a few particles were found at grain boundaries. It is therefore conceivable that TiC_x existing mainly in the form of GB-TiC_x led to the aligned particle distributional pattern, whereas the situation in the form of intragranular TiC_x exhibited the dispersed particle distributional pattern. This observation combined with Figure 2(b) with higher magnification suggests that the intragranular TiC_x particles tend to precipitate at the

bundles of coarse laths of secondary α-phase or their intersections rather than randomly. More detailed discussion combined with synchrotron results is done in section 4.1.

3.3. Mechanical properties:

The main tensile properties associated with particle distribution patterns are illustrated in Figure 4 and the detailed tensile and microstructural properties with average and experimental errors are specified in Table 4. The PIM-parts with fully and partially aligned TiC_x particles basically showed relatively low elongation to fracture (ε_f) (see the left side of Figure 4), whereas the materials with dispersed TiC_x particles provided values for ε_f as high as 8% (right side). Furthermore, elongation in TZN20 series was significantly improved after performing CSRA, but not much by only Y addition. A striking enhancement of ≈113% in elongation was attained from conventional-sintered TZN20 to particle-redistributed TZN20-Y&CSRA. However, ε_f in TZN18 series (reference group) did not exhibit an apparent increase owing to CSRA. It was because the TiC_x particle distributional pattern was already dispersed before CSRA and no obvious change in distribution was found after CSRA.

Ultimate tensile strength (UTS) declined marginally by CSRA in all conditions likely owing to the combination of slight stress relieving and microstructure change, while it was virtually unchanged by Y addition. Moreover, comparing TZN20-Y and TZN18-Y suggests a moderate decline in UTS, around 50 MPa. This strength weakening was basically caused by degraded substitution strengthening effects of Nb. Additionally, the contribution of TiC_x particle reinforcement partially shifting to carbon interstitial strengthening (6.9 MPa/0.01 wt.% C in Ti [57]) on strength remains unclear.

In addition, Young's moduli of the present PIM-TZN alloys (Table 4) were far below the majority of specified titanium alloys [2, 58]. Their β-stabilizer Nb contents are close to the first valley value (the minor Nb content) of Young's modulus in Ti-Nb system [59]. Interestingly, the "neutral element" Zr and "α-stabilizing element" O are by some authors considered to stabilize β-phase when they are added in β titanium alloys [60, 61]. Zr and O are also able to suppress the ω phase and martensitic transformation effecting low Young's modulus [61, 62]. Low moduli can weaken the stress-shielding effects in orthopedic applications.

3.4. Fractography:

In order to reveal the influence of particle distributional patterns of TiC_x on toughness to strain of PIM-TZN alloys, we examined tensile fracture profiles (Figure 5) of TZN20 (aligned particles) and of TZN20-Y&CSRA (dispersed particles). In aligned case in TZN20, particle-fragments were in near-alignment with the fracture edge (see Figure 5(a)). This suggests that before total fracture, these fragments were consistently aligned-agglomerated TiC_x particles distributed along prior β grain boundaries. Moreover, a few torn large-sized cracks were found generally near the fracture edge; a typical interior macro-crack is visible in Figure 5(b). It can be inferred that several cracks were growing concurrently, even so, the majority of cracks remained below the critical crack size. Additionally, porosity is believed to likely facilitate these cracks, because smooth cambered surfaces or arcs can be repeatedly seen at the fracture edge. From Figure 5(c) it can be identified that aligned TiC_x particles were frequently ruptured; the upper arrow pointed out that two cracks were linked and the lower arrow indicated that relatively large cracks were quite close.

The crack growth path in TZN20-Y&CSRA is very winding (see Figure 5(d)). Neither macrocracks similar to Figure 5(b) nor connected microcracks as marked by arrow in Figure

5(c) were discovered in the interior of TZN20-Y&CSRA with dispersed TiC_x (as shown in Figure 5(d)). This implies that very few microcracks grew during plastic deformation. Nonetheless, there is a large amount of ruptured TiC_x particles, which are randomly embedded in the Ti-matrix (see Figure 5(e)). The magnified images of representative ruptured TiC_x particles are given in Figure 5(f); obvious localized plastic deformation and crack-tip blunting, i.e. large crack opening displacement (COD), are visible. Also, multiple cracked TiC_x particles can be found.

On the whole, no pulled-off intact TiC_x particles were discovered. Nor has decohesion at the particle-matrix interface been observed. The appearance of only internal fracture suggests that the cohesion bonding between TiC_x particles and Ti matrix was sufficiently strong. Cracking occurred virtually perpendicular to the tension-loading direction.

The fractographic images support the idea that the present PIM-TZN alloys can be classified into two different fracture modes corresponding to their different particle distribution patterns, as illustrated by Figure 6. It was invariably observed in cases of aligned carbides that numerous platelet-shaped TiC_x particles (fragments) and visible cracks with a particularly large size scattered on the fracture surface occurred, as denoted by arrows in Figure 6(a)-(c). These visible cracks were likely the branches of crack propagation. In general, the fractography in case of aligned particles showed quasi-cleavage planes characterizing a relatively brittle fracture mode, occasionally decorated with several rather shallow dimples. By contrast, PIM-TZN alloys with dispersed TiC_x particles demonstrated a basically ductile fracture mode ($\varepsilon_f \approx 8\%$) with a large number of deep dimples, where plastic slipping bands are visible, as shown in Figure 6(d)-(f). TiC_x fragments were seldom seen in these cases. Fairly small-sized cracks or microvoids can be found in some occasions. All in all, the fracture surface of the aligned particles case exhibits

excessive TiC_x fragments and cracking branches, whereas the dispersed manifests only few fragments but deep dimples.

3.5. In situ high energy X-ray diffraction:

The percentages of TiC_x precipitation of TZN20 and TZN20-Y in relation to the temperature during cooling are plotted in Figure 7. The starting temperature of TiC_x precipitation in the case of the Y containing alloy was much lower than TZN20. Importantly, TiC_x evolution in TZN20 demonstrated a three-step process: a drastic precipitation-type reaction at the start, afterwards a moderate dissolution-type reaction and a re-precipitation reaction towards the end. This moderate dissolution-type reaction corroborates that the high-temperature α phase has a higher solubility of carbon, which is in general agreement with the Ti-C phase diagrams reported in the literature [33, 63]. Corresponding to the phase diagram, the synchrotron results reveal two non-adjacent TiC_x precipitation-type reactions occurring in the high temperature β phase region (Region I) and in the low temperature α + β region (Region III). These regions sandwich a dissolution-type region (Region II) just below α/β transus. At sufficiently low cooling rate (e.g. 2K/min) in the CSRA step or during the synchrotron experiment, the dissolution-type reaction in Region II is extended to longer duration (≈156 min in CSRA, ≈73 min in synchrotron experiment) compared to the conventional sintering cycle (≈15 min) enabling a sufficient dissolution of the carbides formed in Region I. Thus, to some extent, TiC_x was dissolved into the Ti matrix and subsequently reprecipitated at low temperature in Region III. By contrast, the amount of precipitating TiC_x in TZN20-Y increased monotonously and at much lower temperature than TZN20.

4. Discussion

4.1. Particle redistribution behavior:

In this study, it is thought that carbon contamination in PIM technology originates from the sintering atmosphere (main source), the debinding process and the starting powders. These unavoidable carbon contamination sources contribute to aligned GB-TiC$_x$ second-phase precipitation in PIM-TZN alloys processed by a conventional-sintering cycle. It was shown, that performing the combination of Y-addition and CSRA facilitates the adjustment of the distributional pattern of aligned platelet-shaped GB-TiC$_x$ to dispersed spheroidal intragranular TiC$_x$ particles. Additionally, the majority of intragranular TiC$_x$ particles still has a precipitation preference on the bundles of α_s-laths and walls of pores rather than being purely random. This phenomenon is defined as the redistribution behavior of TiC$_x$ phases. Experiments by synchrotron radiation discovered that this combination of Y and CSRA remarkably influences the precipitating evolution of TiC$_x$. The schematic diagram of TiC$_x$ redistribution behavior effected by Y-addition and CSRA is delineated in Figure 8.

An explicit clarification on this TiC$_x$ redistribution mechanism is needed in order to control the TiC$_x$ particle distribution to design appropriate procedures to achieve this. The particle redistribution by CSRA is an interplay between TiC$_x$ dissolution and reprecipitation reactions as elucidated in the following. Above α/β Ti transus (Region I), due to the shrinking of the β-Ti lattice during cooling carbon atoms begin to gather at β-Ti grain boundaries characterized by a number of lattice defects and flaws. This effect is the well-documented precipitation evolution of GB-TiC$_x$ [37, 53, 64]. Carbon atoms in GB-TiC$_x$ are generally released from β-Ti phase, which is the so-called "inherent precipitating parent". As temperature drops below α/β transus (Region II), secondary α-Ti phase grows inside of the prior β-Ti grains [1, 62, 65-67]. The hcp α-Ti phase is able to offer lattice vacancies that are more effective to dissolve carbon

atoms than the interstices provided by bcc β-Ti, as interpreted in the introduction. During sufficiently slow consolidation (e.g. CSRA), carbon atoms that resided in β phase prefer to diffuse into these continuously emerging octahedral vacancies. Simultaneously, GB-TiC$_x$ is dissolved in contiguous unoccupied vacancies, where carbon atoms just left to diffuse towards new voids of α-Ti. In this regard, it is conceivable that "interstitial diffusion" occurred during this carbon diffusion process. In Region II, breaking of Ti-C bonds, growth of acicular secondary α-phases and dissolving GB-TiC$_x$ by α-laths likely take place simultaneously. However, these processes, and the diffusion of carbon atoms from the GBs into the interior of prior β grains, are time-consuming, while the lattice steadily shrinks as the temperature drops. It is associated with the delay of TiC$_x$ precipitation peak, i.e. the peak value is reached slightly later at a lower temperature (see Figure 7) rather than exactly on the α/β transus (810 °C). This process continues until carbon solution capability brought from emerging octahedral voids is counterbalanced by continuous lattice space shrinking due to temperature decrease. Shortly after that, the intragranular TiC$_x$ reprecipitates at significantly lower temperature (Region III). In this case, carbon atoms of intragranular TiC$_x$ mostly are released from the precipitating parent of α-Ti. The intragranular TiC$_x$ is trapped in the bundles of laths of secondary α-Ti (interior of β-Ti), since carbon diffusion rate at low temperature region is by far smaller than in high temperature Region I. This trapping (i.e. slow diffusion) is not only related to relatively low temperature, but also to a structurally lower atomic diffusivity in hcp α-Ti with compact atomic stacking than in bcc β-Ti. Note that α-Ti lath bundles might be a prerequisite for intragranular precipitation, in addition to sufficient carbon source for TiC$_x$ particle nucleation and growth. Hence, it is assumed that this CSRA method is limited to metastable β titanium with a certain fraction of secondary α-Ti; full β titanium and its alloys with very less secondary α-Ti might be not appropriate for designing a special sintering cycle.

The redistribution behavior after adding Y is likely effected by the much lower precipitating temperature of TiC_x. Consequently, the extremely low diffusion rate of carbon atoms is a strong barrier for forming of $GB-TiC_x$ on the exterior of β-Ti grains. As reported by Chen et al. [37], intragranular TiC_x particles were observed in β-Ti alloys containing Ta and V as β-stabilizers. It was claimed that owing to their larger lattice vacancies, carbon atoms can remain as solved in Ti matrix during the cooling procedure until a relatively low temperature is reached, where TiC_x begins to precipitate. A possible explanation for lowering the precipitating temperature of TiC_x by Y could be that both Y and TiC_x are oxygen getters. In principle, 0.1 wt.% Y getter can scavenge up to 60 at.% of oxygen, while 0.5 wt.% TiC_x getter basically contains below 10 at.% oxygen [52]. It seems to indicate that the solubility of carbon at high temperatures in titanium alloys can be affected by the oxygen concentration of Ti-matrix. Oxygen atoms in grain boundaries, in turn, are likely necessary for the formation of $GB-TiC_x$. However, grain boundary oxygen is easily scavenged by yttrium due to short-circuit diffusion. In this case, TiC_x may nucleate elsewhere, e.g. on the walls of porosity with a relatively high oxygen content and lattice flaws. This influence will be investigated in more detail in future work.

4.2. Microcrack initiation and crack propagation mechanisms in different TiC_x distributional patterns:

We have shown that two strikingly different tensile fracture behaviors occur in PIM-TZN alloys with aligned-agglomerated and evenly-dispersed TiC_x particle distributional patterns. The aligned pattern strongly degrades elongation to fracture in comparison to the dispersed case. It has been fairly well-established in this article that worst-case "early-existing" microcracks initiate in TiC_x particles and the cracking coalesces the continuously aligned $GB-TiC_x$ particles via two damage mechanisms.

4.2.1. Microcracks initiation mechanism

Cracking is hardly ever found in the soft Ti-matrix away from TiC_x; only microcracks exist either in a singular particle (dispersed TiC_x) or frequently connected between GB-TiC_x particles (aligned TiC_x). The critical cracking of the whole specimen is invariably originated from TiC_x. No microvoids or other types of defects of the β Ti-matrix could be found as possible crack initiation sites; while the ruptured TiC_x particles work as worst-case "early-existing" microcracks responsible for fracture of the whole specimen.

Previous studies have shown that the tensile fracture of PIMed Ti-Nb is accompanied by a large number of ruptured TiC_x already at as low tensile strains as 1.4% [41, 68]. Analogously, in the literature [69, 70], it even has been found via *in situ* microscopy that TiC particles and TiB whiskers begin to crack even before reaching the overall yield stress in unalloyed titanium. Thus, it can be assumed that TiC_x particles in present PIM-TZN alloys begin to fracture early at a rather low strain. This is because of load-sharing effects transferring force from the soft Ti-matrix to the stiff TiC_x [71, 72] (≈180 GPa in carbon-deficient carbides [33]). Due to the brittle nature and the high crystallographic symmetry of TiC_x, a rapid through-thickness cracking occurring in TiC_x particle is easily fulfilled; the formation of such crack is a sign of microcrack initiation of the whole PIM-TZN material.

Multiple cracking (e.g. see Figure 5(f)) of TiC_x particle is possibly a consequence of dislocation pileups (local stress concentration). These dislocation pile-ups were mainly generated from i) geometrically necessary dislocations arising from strain incompatibility, ii) processing residuals and iii) dislocation loops from TiC_x barriers to Ti-matrix plastic deformation migration and dislocation flow [73-75]. Both the premier microcracks and repeated

cracks of TiC$_x$ basically possess the same potential to contribute to crack coalescence propagation in the whole material.

4.2.2. The mechanisms of crack propagation modes in PIM-TZN alloys with aligned GB-TiC$_x$ and dispersed intragranular TiC$_x$

A great amount of apparent crack-tips blunting or large COD (crack opening displacement) ahead of "early-existing" microcracks indicates that crack propagation was pinned within stiff TiC$_x$ particles rather than immediately penetrating the particle-matrix bonding interface to continue into the soft Ti-matrix. Large COD is the consequence of severe localized plastic strain of Ti-matrix emanated from crack-tips. Providing such large localized plastic deformation suggests the β matrix of PIM-TZN possesses a good inherent toughness.

In general, there exist distinctly different thresholds for crack propagation in ductile Ti-matrix and brittle ceramic TiC$_x$-particles [76-78]. The trigger of crack propagation in ductile metals can be expressed by A. Wells empirical equation based on elastic-plastic fracture model [79].

$$\delta = 2\pi e a_i$$

Where δ the constant of ductile materials is the critical COD, e is nominal strain and a_i is initial crack length, i.e. the ruptured TiC$_x$ in this study.

Therefore, this large COD ahead of "early-existing" microcracks means that a large nominal strain e is required to trigger cracking propagation. Furthermore, it is widely recognized that titanium alloys have a rather low work-hardening rate. As a paradox, this is advantageous to restrict stress intensification ahead of crack-tips, but simultaneously leads to severe strain localization [43]. This synergy results in the observed localized severe plastic deformation

ahead of crack-tips. With the strain increasing, when the critical COD is reached, "early-existing" microcracks eventually cause decohesion of the metallic bonds in β-matrix. Then, these microcracks, which were trapped in TiC_x particles, now propagate into the soft β matrix.

For the cases of aligned $GB\text{-}TiC_x$ particles, crack propagation preferred to act by connecting the continuously aligned "early-existing" microcracks. In brief, this is a combination of crack propagation modes containing microcracks coalescence mode and crystal defects cleavage fracture mode. Their detailed mechanisms are given here. First of all, there are a relatively high impurity level (Fe, P, Cl, S and so forth [80]) and microstructural lattice defects in grain boundaries, which typically offer significantly poorer atomic bonding. Furthermore, crack coalescence commonly seeks the shortest path to link these "early-existing" cracks due to the lowest tearing energy consumption. Therefore, it is theoretically impossible that the critical crack bypassed these "early-existing" cracks (voids) in GBs and tore the strongly atomically bonded Ti-matrix. This combination of fracture modes observed here is in exceptionally good agreement with existing intrinsic mechanisms of damage promoting crack advance [43, 81].

By contrast, in evenly-dispersed particle distribution paths to connect "early-existing" microcracks are more twisting and require an appreciable tearing energy. Moreover, the crack bridging effect and atomic bonding in the interior of β-grains are strong. Thus, those two negative crack propagation modes are difficult to run in PIM-TZN with evenly-dispersed TiC_x particle distribution. Because strength is nearly equivalent, the toughness behaviors of PIM-TZN alloys with different TiC_x particle distribution patterns can be mirrored to elongation to fracture (ε_f) from 3.9% in the aligned TiC_x cases to 8.3% in the dispersed ones. From the comparison of the tensile properties in Figure 9, the elongation of TiC_x-redistributed TZN20 is much higher than the majority of reported PIM β titanium alloys [41, 42, 68, 82-87]. Compared

with pre-alloyed powder method prepared Ti-24Nb-4Zr-8Sn [42] and Ti-15V-3Al-3Sn-3Cr [83] with the same level of elongation, it could offer a 120−180 MPa higher tensile strength.

4.3. The extra effects of CSRA and Y on Ti-matrix except for TiC$_x$ redistribution:

In order to ascertain the practical impact of particle redistribution on tensile toughening from all possible impact factors, we took extra effects of these TiC$_x$ redistribution methods into consideration. It is separately illustrated in this section.

The prolonged exposure to a rather high temperature during CSRA might have an influence on Ti-matrix, e.g. very slight stress relieving on the basis of very low as-sintered residual stress. In this study, in order to distinguish extra effects, the same CSRA step was applied to the reference group TZN18-Y(&CSRA). Both variants with dispersed TiC$_x$ were basically equal in terms of particle distribution pattern because of a low TiC$_x$ fraction (see Table 1). An evaluation of the toughening (improvement of ε_f) mechanisms in PIM-TZN alloys after CSRA is tried in Figure 10. We only can see a negligible increment of elongation in the reference group. It is evident from the results that TiC$_x$ redistribution behavior induced by CSRA contributes mainly to the toughening effect in TZN20 series.

Extra effects in microstructural-scale related to Y addition are summarized in Table 5. The porosity, oxygen level and prior β grain size were slightly altered (see the lower half of Table 5). The early-formed large yttria particles obstruct material diffusion in sintering, resulting in porosity increasing. Generally acknowledged, porosity is detrimental to tensile elongation. Thus, especially large-sized elemental Y powder should be used deliberately. The addition of 0.1 wt.% yttrium could scavenge oxygen atoms and the resulting slightly lower oxygen level (0.027 wt.%) of Ti-matrix may improve ductility [55]. Nonetheless, it has been widely accepted

that β Ti alloys can tolerate a relatively higher oxygen concentration (≈0.8 wt.%) without a slump in elongation [26]. Thus, the effects of a possible decrease in oxygen level in this case might be insignificant. In addition, a smaller average grain size suppress crack initiation, whereas the large grain size could resist crack growth, which is more important in toughening [88]. Consequently, a quite negative effect on porosity brought from Y addition is likely to offset a certain degree of improvement on elongation arising from TiC_x redistribution behavior.

5. Conclusions

Metastable β-type Ti-Nb-Zr biotolerant materials were fabricated using powder injection molding (PIM) with 0.05 wt.% carbon residuals, which is a normal carbon contamination level for Ti-PIM. Examining for carbon contamination sources of this binder-based powder technology shows that improper thermal pyrolysis of polymers is not as critical as normally assumed. Instead, carbon uptake from sintering atmosphere is found more likely to play a significant role.

TiC_x redistribution methods first proposed in this article, i.e. the combination of trace yttrium addition (Y) and carbide spheroidization reprecipitation annealing (CSRA), changed an aligned TiC_x distribution (obtained by conventional sintering program) to a dispersed TiC_x distribution in PIM-processed Ti-Nb-Zr alloys. It is found by EBSD that this adjustment of particle distributional patterns means, essentially, that aligned TiC_x particles along grain boundaries (GB-TiC_x) are transferred to the interior of β-grains to form dispersed intragranular TiC_x. Synchrotron radiation experiments reveal that Y lowers the initial precipitation temperature of TiC_x, while CSRA effects that partial GB-TiC_x second-phases are dissolved within Ti-matrix to reprecipitate at a much lower temperature; thereby generating a higher fraction of intragranular TiC_x via these methods.

Tensile toughness behaviors of PIM-TZN alloys with aligned and dispersed TiC_x particle distributional patterns are significantly different. The alloys with aligned GB-TiC_x exhibit premature intergranular fracture ($\varepsilon_f = 3.9\%$), whereas the alloys with dispersed TiC_x manifest a striking enhancement on toughness ($\approx113\%$ increment in ε_f to 8.3%, the strengths remain nearly equivalent). Inspections of fracture modes indicate that prematurely ruptured TiC_x particles work as worst-case "early-existing" microcracks and crack propagation modes (incl.

microcracks coalescence mode and crystal defects cleavage fracture mode) occur in these aligned "early-existing" microcracks in GBs as the dominant crack growth mechanism at rather low strain. The low tearing energy of these two negative crack growth modes causes low toughness of the alloys with aligned GB-TiC_x. Dispersed intragranular TiC_x particles request more winding crack growth and possess stronger atomic bonding in the interior of β-grains than at GBs, acting as intrinsic toughening mechanisms. A novel toughening strategy to adjust particle distribution pattern (TiC_x phases redistribution) by regulating the precipitation evolution of TiC_x was successfully established. TiC_x redistribution methods aiming to eliminate aligned GB-TiC_x particles can be applied to effectively toughen powder metallurgical β titanium alloys suffered from embrittlement induced by carbon contamination.

Data availability

The raw/processed data required to reproduce these findings cannot be shared at this time as the data also forms part of an ongoing study.

References

[1] F. Froes, H. Bomberger, The beta titanium alloys, JOM 37(7) (1985) 28-37.

[2] M. Niinomi, Mechanical properties of biomedical titanium alloys, Materials Science and Engineering: A 243(1-2) (1998) 231-236.

[3] M. Niinomi, T. Kobayashi, Toughness and strength of microstructurally controlled titanium alloys, ISIJ international 31(8) (1991) 848-855.

[4] T. Saito, T. Furuta, J.-H. Hwang, S. Kuramoto, K. Nishino, N. Suzuki, R. Chen, A. Yamada, K. Ito, Y. Seno, Multifunctional alloys obtained via a dislocation-free plastic deformation mechanism, Science 300(5618) (2003) 464-467.

[5] M. Geetha, A.K. Singh, R. Asokamani, A.K. Gogia, Ti based biomaterials, the ultimate choice for orthopaedic implants–a review, Progress in materials science 54(3) (2009) 397-425.

[6] K. Wang, The use of titanium for medical applications in the USA, Materials Science and Engineering: A 213(1-2) (1996) 134-137.

[7] M. Long, H. Rack, Titanium alloys in total joint replacement—a materials science perspective, Biomaterials 19(18) (1998) 1621-1639.

[8] Y. Okazaki, S. Rao, Y. Ito, T. Tateishi, Corrosion resistance, mechanical properties, corrosion fatigue strength and cytocompatibility of new Ti alloys without Al and V, Biomaterials 19(13) (1998) 1197-1215.

[9] H. Matsuno, A. Yokoyama, F. Watari, M. Uo, T. Kawasaki, Biocompatibility and osteogenesis of refractory metal implants, titanium, hafnium, niobium, tantalum and rhenium, Biomaterials 22(11) (2001) 1253-1262.

[10] A. Biesiekierski, J. Wang, M.A.-H. Gepreel, C. Wen, A new look at biomedical Ti-based shape memory alloys, Acta biomaterialia 8(5) (2012) 1661-1669.

[11] M. Niinomi, Fatigue performance and cyto-toxicity of low rigidity titanium alloy, Ti–29Nb–13Ta–4.6 Zr, Biomaterials 24(16) (2003) 2673-2683.

[12] E. Eisenbarth, D. Velten, M. Müller, R. Thull, J. Breme, Biocompatibility of β-stabilizing elements of titanium alloys, Biomaterials 25(26) (2004) 5705-5713.

[13] Y. Okazaki, E. Gotoh, Comparison of metal release from various metallic biomaterials in vitro, Biomaterials 26(1) (2005) 11-21.

[14] A. Fukuda, M. Takemoto, T. Saito, S. Fujibayashi, M. Neo, S. Yamaguchi, T. Kizuki, T. Matsushita, M. Niinomi, T. Kokubo, Bone bonding bioactivity of Ti metal and Ti–Zr–Nb–Ta alloys with Ca ions incorporated on their surfaces by simple chemical and heat treatments, Acta Biomaterialia 7(3) (2011) 1379-1386.

[15] G. Yang, T. Zhang, Phase transformation and mechanical properties of the Ti50Zr30Nb10Ta10 alloy with low modulus and biocompatible, Journal of Alloys and Compounds 392(1-2) (2005) 291-294.

[16] H. Kim, Y. Ikehara, J. Kim, H. Hosoda, S. Miyazaki, Martensitic transformation, shape memory effect and superelasticity of Ti–Nb binary alloys, Acta Materialia 54(9) (2006) 2419-2429.

[17] Q. Li, M. Niinomi, J. Hieda, M. Nakai, K. Cho, Deformation-induced ω phase in modified Ti–29Nb–13Ta–4.6 Zr alloy by Cr addition, Acta biomaterialia 9(8) (2013) 8027-8035.

[18] D.F. Heaney, Handbook of metal injection molding, Elsevier2012.

[19] G. Wen, P. Cao, B. Gabbitas, D. Zhang, N. Edmonds, Development and design of binder systems for titanium metal injection molding: An overview, Metallurgical and Materials Transactions A 44(3) (2013) 1530-1547.

[20] T. Ebel, V. Friederici, P. Imgrund, T. Hartwig, Metal injection molding of titanium, Titanium powder metallurgy, Elsevier2015, pp. 337-360.

[21] Z.Z. Fang, J.D. Paramore, P. Sun, K.R. Chandran, Y. Zhang, Y. Xia, F. Cao, M. Koopman, M. Free, Powder metallurgy of titanium–past, present, and future, International Materials Reviews 63(7) (2018) 407-459.

[22] E. Baril, L. Lefebvre, Y. Thomas, Interstitial elements in titanium powder metallurgy: sources and control, Powder metallurgy 54(3) (2011) 183-186.

[23] R. German, Progress in titanium metal powder injection molding, Materials 6(8) (2013) 3641-3662.

[24] A. Dehghan-Manshadi, M. Bermingham, M. Dargusch, D. StJohn, M. Qian, Metal injection moulding of titanium and titanium alloys: Challenges and recent development, Powder technology 319 (2017) 289-301.

[25] J.C. Slater, Atomic radii in crystals, The Journal of Chemical Physics 41(10) (1964) 3199-3204.

[26] M. Yan, W. Xu, M. Dargusch, H. Tang, M. Brandt, M. Qian, Review of effect of oxygen on room temperature ductility of titanium and titanium alloys, Powder Metallurgy 57(4) (2014) 251-257.

[27] R. Jaffee, H. Ogden, D. Maykuth, Alloys of titanium with carbon, oxygen, and nitrogen, JOM 2(10) (1950) 1261-1266.

[28] H. Conrad, Effect of interstitial solutes on the strength and ductility of titanium, Progress in Materials Science 26(2-4) (1981) 123-403.

[29] M. Chandran, P. Subramanian, M.F. Gigliotti, Energetics of interstitial oxygen in β-TiX (X= transition elements) alloys using first principles methods, Journal of Alloys and Compounds 571 (2013) 107-113.

[30] S.C. Tjong, Y.-W. Mai, Processing-structure-property aspects of particulate-and whisker-reinforced titanium matrix composites, Composites Science and Technology 68(3-4) (2008) 583-601.

[31] K. Cho, M. Niinomi, M. Nakai, H. Liu, P.F. Santos, Y. Itoh, M. Ikeda, T. Narushima, Improvement in mechanical strength of low-cost β-type Ti–Mn alloys fabricated by metal injection molding through cold rolling, Journal of Alloys and Compounds 664 (2016) 272-283.

[32] T. Ebel, T. Beißig, S. Ebner, X. Luo, A.B. Nagaram, D. Zhao, Reduction of the embrittlement effect of binder contamination in MIM processing of Ti alloys, Powder Metallurgy 60(3) (2017) 157-166.

[33] M. Yan, M. Qian, C. Kong, M. Dargusch, Impacts of trace carbon on the microstructure of as-sintered biomedical Ti–15Mo alloy and reassessment of the maximum carbon limit, Acta biomaterialia 10(2) (2014) 1014-1023.

[34] W. Weng, A. Biesiekierski, Y. Li, C. Wen, Effects of selected metallic and interstitial elements on the microstructure and mechanical properties of beta titanium alloys for orthopedic applications, Materialia (2019) 100323.

[35] D. Konitzer, M. Loretto, Microstructural assessment of Ti6A14V-TiC metal-matrix composite, Acta Metallurgica 37(2) (1989) 397-406.

[36] P. Wanjara, R. Drew, J. Root, S. Yue, Evidence for stable stoichiometric Ti2C at the interface in TiC particulate reinforced Ti alloy composites, Acta materialia 48(7) (2000) 1443-1450.

[37] Z. Chen, Y. Li, M. Loretto, Role of alloying elements in microstructures of beta titanium alloys with carbon additions, Materials science and technology 19(10) (2003) 1391-1398.

[38] V. Moisy-Maurice, N. Lorenzelli, C. De Novion, P. Convert, High temperature neutron diffraction study of the order-disorder transition in TiC1− x, Acta Metallurgica 30(9) (1982) 1769-1779.

[39] H. Goretzki, Neutron diffraction studies on titanium-carbon and zirconium-carbon alloys, physica status solidi (b) 20(2) (1967) K141-K143.

[40] D.B. Miracle, H.A. Lipsitt, Mechanical Properties of Fine-Grained Substoichiomebic Titanium Carbide, Journal of the American Ceramic Society 66(8) (1983) 592-597.

[41] D. Zhao, K. Chang, T. Ebel, H. Nie, R. Willumeit, F. Pyczak, Sintering behavior and mechanical properties of a metal injection molded Ti–Nb binary alloy as biomaterial, Journal of Alloys and Compounds 640 (2015) 393-400.

[42] F. Kafkas, T. Ebel, Metallurgical and mechanical properties of Ti–24Nb–4Zr–8Sn alloy fabricated by metal injection molding, Journal of Alloys and Compounds 617 (2014) 359-366.

[43] M.E. Launey, R.O. Ritchie, On the fracture toughness of advanced materials, Advanced Materials 21(20) (2009) 2103-2110.

[44] L. Huang, L. Geng, H. Peng, Microstructurally inhomogeneous composites: is a homogeneous reinforcement distribution optimal?, Progress in Materials Science 71 (2015) 93-168.

[45] T. Tingskog, F. Larouche, L.-P. Lefebvre, New Titanium Alloy Feedstock for High Performance Metal Injection Molding Parts, Key Engineering Materials 704 (2016).

[46] I. Sabirov, O. Kolednik, R. Valiev, R. Pippan, Equal channel angular pressing of metal matrix composites: effect on particle distribution and fracture toughness, Acta Materialia 53(18) (2005) 4919-4930.

[47] S. Gorsse, D.B. Miracle, Mechanical properties of Ti-6Al-4V/TiB composites with randomly oriented and aligned TiB reinforcements, Acta Materialia 51(9) (2003) 2427-2442.

[48] C. Schulze, M. Weinmann, C. Schweigel, O. Keßler, R. Bader, Mechanical properties of a newly additive manufactured implant material based on Ti-42Nb, Materials 11(1) (2018) 124.

[49] M. Sato, M.A. Sambito, A. Aslani, N.M. Kalkhoran, E.B. Slamovich, T.J. Webster, Increased osteoblast functions on undoped and yttrium-doped nanocrystalline hydroxyapatite coatings on titanium, Biomaterials 27(11) (2006) 2358-2369.

[50] F. Feyerabend, J. Fischer, J. Holtz, F. Witte, R. Willumeit, H. Drücker, C. Vogt, N. Hort, Evaluation of short-term effects of rare earth and other elements used in magnesium alloys on primary cells and cell lines, Acta biomaterialia 6(5) (2010) 1834-1842.

[51] O.I. Velikokhatnyi, P.N. Kumta, First-principles studies on alloying and simplified thermodynamic aqueous chemical stability of calcium-, zinc-, aluminum-, yttrium-and iron-doped magnesium alloys, Acta Biomaterialia 6(5) (2010) 1698-1704.

[52] M. Qian, F.H. Froes, Titanium powder metallurgy: science, technology and applications, Butterworth-Heinemann2015.

[53] D.P. Zhao, K.K. Chang, T. Ebel, M. Qian, R. Willumeit, M. Yan, F. Pyczak, Titanium carbide precipitation in Ti-22Nb alloy fabricated by metal injection moulding, Powder Metallurgy 57(1) (2014) 2-4.

[54] P.F. Santos, M. Niinomi, K. Cho, H. Liu, M. Nakai, T. Narushima, K. Ueda, Y. Itoh, Effects of Mo addition on the mechanical properties and microstructures of Ti-Mn alloys fabricated by metal injection molding for biomedical applications, Materials transactions 58(2) (2017) 271-279.

[55] W. Limberg, T. Ebel, Metal Injection Moulding of Ti-6Al-4V with Yttrium addition, Key Engineering Materials 704 (2016).

[56] W. Pearson, A Handbook of Lattice spacings and Structures of Metals and Alloys Pergarnon Press, Oxfrd, 1964.

[57] H. Ogden, R. Jaffee, The effects of carbon, oxygen, and nitrogen on the mechanical properties of titanium and titanium alloys, Battelle Memorial Inst. Titanium Metallurgical Lab., Columbus, Ohio, 1955.

[58] M. Niinomi, M. Nakai, J. Hieda, Development of new metallic alloys for biomedical applications, Acta biomaterialia 8(11) (2012) 3888-3903.

[59] T. Ozaki, H. Matsumoto, S. Watanabe, S. Hanada, Beta Ti alloys with low Young's modulus, Materials transactions 45(8) (2004) 2776-2779.

[60] M. Abdel-Hady, H. Fuwa, K. Hinoshita, H. Kimura, Y. Shinzato, M. Morinaga, Phase stability change with Zr content in β-type Ti–Nb alloys, Scripta Materialia 57(11) (2007) 1000-1003.

[61] M. Abdel-Hady, K. Hinoshita, M. Morinaga, General approach to phase stability and elastic properties of β-type Ti-alloys using electronic parameters, Scripta Materialia 55(5) (2006) 477-480.

[62] D. Banerjee, J. Williams, Perspectives on titanium science and technology, Acta Materialia 61(3) (2013) 844-879.

[63] A. International, A.I.A.P.D. Committee, A.I.H. Committee, ASM handbook, ASM International1992.

[64] X. Luo, T. Ebel, F. Pyczak, W. Limberg, Y. Lin, Carbide evolution and its potential reduction methods in Ti-22Nb based alloys prepared by metal injection moulding, Materials Letters 193 (2017) 295-298.

[65] M. Yan, Microstructural characterization of as-sintered titanium and titanium alloys, Titanium powder metallurgy, Elsevier2015, pp. 555-578.

[66] S. Balachandran, A. Kashiwar, A. Choudhury, D. Banerjee, R. Shi, Y. Wang, On variant distribution and coarsening behavior of the α phase in a metastable β titanium alloy, Acta Materialia 106 (2016) 374-387.

[67] S. Van Bohemen, A. Kamp, R. Petrov, L. Kestens, J. Sietsma, Nucleation and variant selection of secondary α plates in a β Ti alloy, Acta Materialia 56(20) (2008) 5907-5914.

[68] D. Zhao, K. Chang, T. Ebel, M. Qian, R. Willumeit, M. Yan, F. Pyczak, Microstructure and mechanical behavior of metal injection molded Ti–Nb binary alloys as biomedical material, Journal of the mechanical behavior of biomedical materials 28 (2013) 171-182.

[69] C. Boehlert, C. Cowen, S. Tamirisakandala, D. McEldowney, D. Miracle, In situ scanning electron microscopy observations of tensile deformation in a boron-modified Ti–6Al–4V alloy, Scripta Materialia 55(5) (2006) 465-468.

[70] S. Li, K. Kondoh, H. Imai, B. Chen, L. Jia, J. Umeda, Y. Fu, Strengthening behavior of in situ-synthesized (TiC–TiB)/Ti composites by powder metallurgy and hot extrusion, Materials & Design 95 (2016) 127-132.

[71] M. Piggott, Load bearing fibre composites, Springer Science & Business Media2002.

[72] G. Garces, G. Bruno, A. Wanner, Load transfer in short fibre reinforced metal matrix composites, Acta Materialia 55(16) (2007) 5389-5400.

[73] M. Ashby, A. Kelly, Strengthening methods in crystals, Elsevier, Amsterdam (1971) 137.

[74] M. Ashby, Deformation of Plastically Non-Homogeneous Alloys, Strengthening Methods in Crystals, 1971, 137-192 (1971).

[75] T. Srivatsan, W. Soboyejo, R. Lederich, Tensile deformation and fracture behaviour of a titanium-alloy metal-matrix composite, Composites Part A: Applied Science and Manufacturing 28(4) (1997) 365-376.

[76] A.A. Wells, Application of Fracture Mechanics to Yielding Materials, Proc R Soc Lon Ser-A 285(1400) (1965) 34-&.

[77] A. Wells, F. Burdekin, Discussion:"On the sharpness of cracks compared with Wells's COD, by JE Srawley, JL Swedlow, and E. Roberts, Jr, International Journal of Fracture Mechanics 7(2) (1971) 233-241.

[78] F. Burdekin, M. Dawes, Conf. on Partica Appl. of Fracture Mech, to Press, Vessel Tech, 1971.

[79] A. Wells, Notched bar tests, fracture mechanics and the brittle strengths of welded structures, British Welding Journal 12(1) (1965) 2.

[80] M. Yan, S. Luo, G. Schaffer, M. Qian, Impurity (Fe, Cl, and P)-induced grain boundary and secondary phases in commercially pure titanium (CP-Ti), Metallurgical and Materials Transactions A 44(8) (2013) 3961-3969.

[81] R.O. Ritchie, Mechanisms of fatigue-crack propagation in ductile and brittle solids, International journal of Fracture 100(1) (1999) 55-83.

[82] D.P. Zhao, Y.K. Chen, K.K. Chang, T. Ebel, B.J.C. Luthrigner-Feyerabend, R. Willumeit-Romer, F. Pyczak, Surface topography and cytocompatibility of metal injection molded Ti-22Nb alloy as biomaterial, T Nonferr Metal Soc 28(7) (2018) 1342-1350.

[83] T. Ebel, O. Ferri, Processing of Ti-15V-3Al-3Sn-3Cr by metal injection moulding, Proceedings of EuroPM, 2011, pp. 265-270.

[84] W. Xu, X. Lu, L. Wang, Z. Shi, S. Lv, M. Qian, X. Qu, Mechanical properties, in vitro corrosion resistance and biocompatibility of metal injection molded Ti-12Mo alloy for dental applications, Journal of the mechanical behavior of biomedical materials 88 (2018) 534-547.

[85] J.-E. Bidaux, F. Comby, M. Rodriguez-Arbaizar, H. Girard, E. Carreño-Morelli, Powder Injection Moulding of Low Modulus Ti-13Nb-13Zr for Implant Application, European Congress and Exhibition on Powder Metallurgy. European PM Conference Proceedings, The European Powder Metallurgy Association, 2016, pp. 1-6.

[86] J.-E. Bidaux, R. Pasquier, M. Rodriguez-Arbaizar, H. Girard, E. Carreño-Morelli, Low elastic modulus Ti–17Nb processed by powder injection moulding and post-sintering heat treatments, Powder Metallurgy 57(5) (2014) 320-323.

[87] E. Endo, H. Nakayama, H. Kyogoku, Effect of Sintering Conditions on Microstructures and Mechanical Properties of Ti-29Nb-13Ta-4.6 Zr Alloy Fabricated by MIM Process, European Congress and Exhibition on Powder Metallurgy. European PM Conference Proceedings, The European Powder Metallurgy Association, 2016, pp. 1-5.

[88] C. Leyens, M. Peters, Titanium and titanium alloys: fundamentals and applications, John Wiley & Sons2003.

Table 1

Impurity levels and TiC$_x$ volume fraction of as-sintered and CSRAed PIM-TZN alloys.

Samples	Carbon/ wt.%	Oxygen/ wt.%	Nitrogen/ wt.%	TiC$_x$ fraction/ %
TZN20	0.047 ± 0.003	0.265 ± 0.001	0.082 ± 0.003	0.53 ± 0.05
TZN20-CSRA[1]	0.049 ± 0.002	0.258 ± 0.004	0.085 ± 0.005	0.51 ± 0.04
TZN20-Y[2]	0.053 ± 0.005	0.249 ± 0.010	0.076 ± 0.007	0.48 ± 0.10
TZN20-Y&CSRA[3]	0.043 ± 0.002	0.245 ± 0.006	0.050 ± 0.006	0.50 ± 0.09
TZN18-Y[2]	0.043 ± 0.011	0.275 ± 0.003	0.076 ± 0.002	0.25 ± 0.05
TZN18-Y&CSRA[3]	0.042 ± 0.003	0.279 ± 0.004	0.079 ± 0.002	0.24 ± 0.08

[1] CSRA has an extra sintering cycle step, which was programmed after the conventional sintering cycle.

[2] 0.1 wt.% yttrium powder was added into the metallic powder mixture.

[3] Both CSRA and Y processes were carried out.

Table 2

Carbon residuals of powder metallurgical TZN20(-Y) specimens under various conditions.

Sample type	Conditions	TZN20/ wt.%	TZN20-Y/ wt.%
i) Starting materials	unsintered	0.007 ± 0.001	0.007 ± 0.001
ii) Pressed and sintered parts	binderless (≈10% sintered porosity)	0.070 ± 0.002	0.068 ± 0.004
iii) PIM-processed parts	binder-based (5−6% sintered porosity)	0.047 ± 0.003	0.053 ± 0.004

Table 3

EDS quasi-quantitive chemical analyses of TiC$_x$ with different particle distributional patterns determined for 10 spots.

Distributional pattern	Samples	C/ at.%	O/ at.%	Ti/ at.%	Nb/ at.%	Zr/ at.%
Aligned TiC$_x$	TZN20	15.7 ± 0.9	6.4 ± 0.7	68.3 ± 0.9	1.7 ± 0.6	7.9 ± 0.8
Dispersed TiC$_x$	TZN20-Y&CSRA	16.8 ± 1.5	5.3 ± 1.2	66.7 ± 2.2	2.0 ± 0.8	9.2 ± 1.5

Table 4

Tensile and microstructural properties of PIM-TZN alloys at room temperature.

Samples	σ_{YS} / MPa	σ_{UTS} / MPa	Elongation (ε_f)/ %	E-Modulus / GPa	Grain size / μm	Porosity / %
TZN20	768 ± 3.9	889 ± 3.9	3.9 ± 0.5	70.9 ± 2.9	373 ± 12	5.0
TZN20-CSRA	704 ± 1.6	822 ± 1.0	5.8 ± 0.4	75.3 ± 3.3	384 ± 16	5.0
TZN20-Y	779 ± 0.9	885 ± 1.2	4.5 ± 0.3	68.5 ± 2.4	301 ± 19	6.0
TZN20-Y&CSRA	742 ± 4.1	832 ± 2.1	8.3 ± 0.6	65.7 ± 4.6	317 ± 15	6.0
TZN18-Y	708 ± 3.3	836 ± 2.2	7.9 ± 0.2	78.4 ± 1.2	325 ± 5	5.5
TZN18-Y&CSRA	681 ± 4.6	783 ± 4.8	8.2 ± 0.3	76.9 ± 5.7	340 ± 21	5.5

Table 5

Sketch of multiple impact factors of Y addition linked to tensile toughness (ε_f represents here) of PIM-TZN20 from various aspects with respect to TiC$_x$-particle and Ti-matrix.

Aspect	Impact factor	TZN20 (ε_f = 3.9%)	TZN20-Y (ε_f = 4.5%)
TiC$_x$ particle	Volume fraction	0.53 vol.%	0.48 vol.%
	Mean particle size	6.6 μm	5.8 μm
	Mean aspect ratio/ unitless	2.55	2.28
	Particle distributional pattern	basically aligned	partially aligned
	Location of precipitation	basically along GBs	partially along GBs
Ti matrix	Porosity	5.0%	6.0%
	Oxygen in solid solution[4]	0.265 wt.%	0.224 wt.%
	Prior β-grain size	373 μm	301 μm
	Secondary α-phase morphology	fine, acicular	fine, acicular

[4] 0.1 wt.% Y particles can scavenge ≈0.027 wt.% O atoms from Ti-matrix to form yttria (Y_2O_3) during the sintering process. Therefore, the oxygen in solid solution decreased in TZN20-Y.

Figure 1:
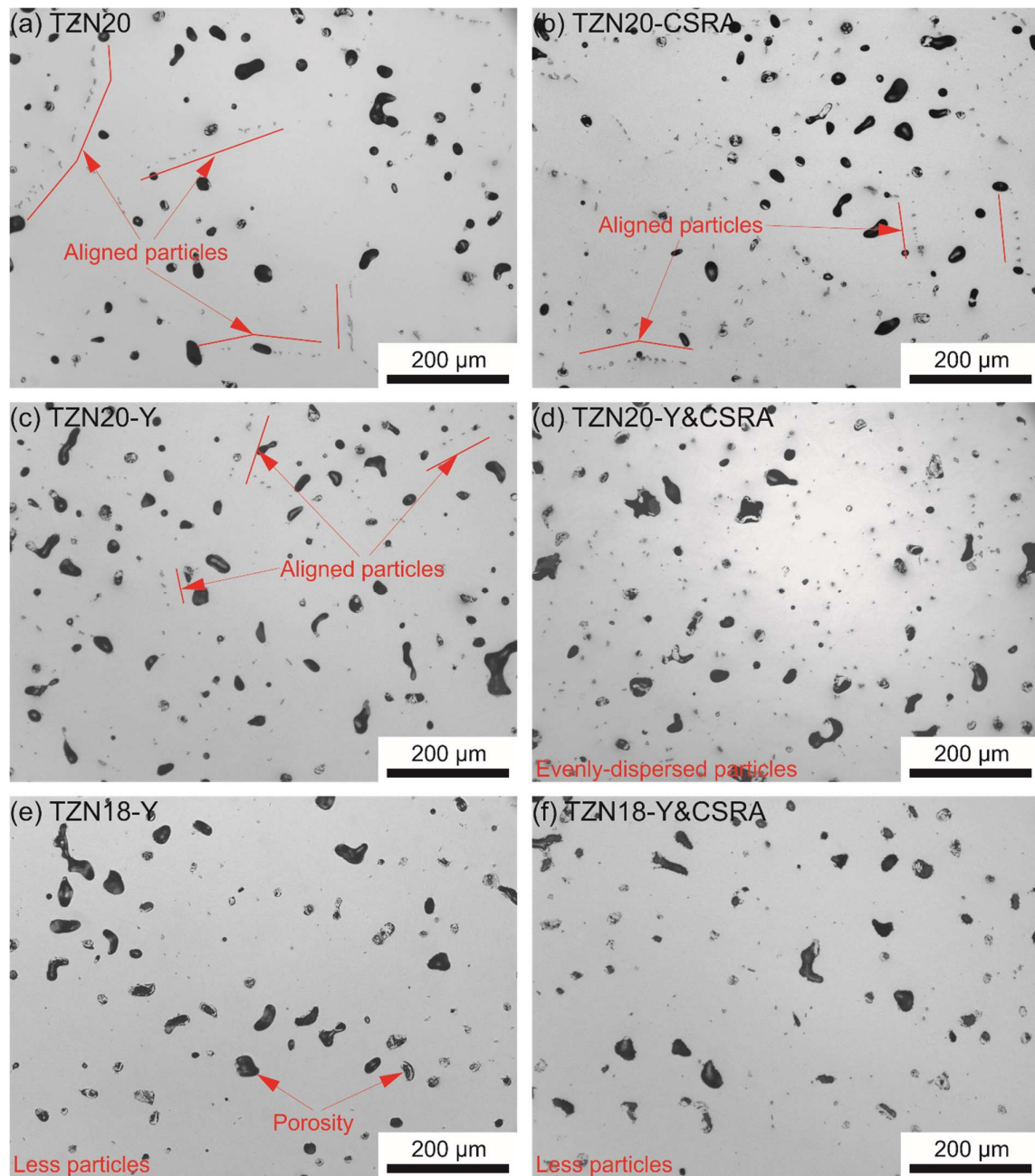
Figure 1 – Optical micrographs of metastable β PIM-TZN alloys with different particle distributional patterns.

Figure 2:
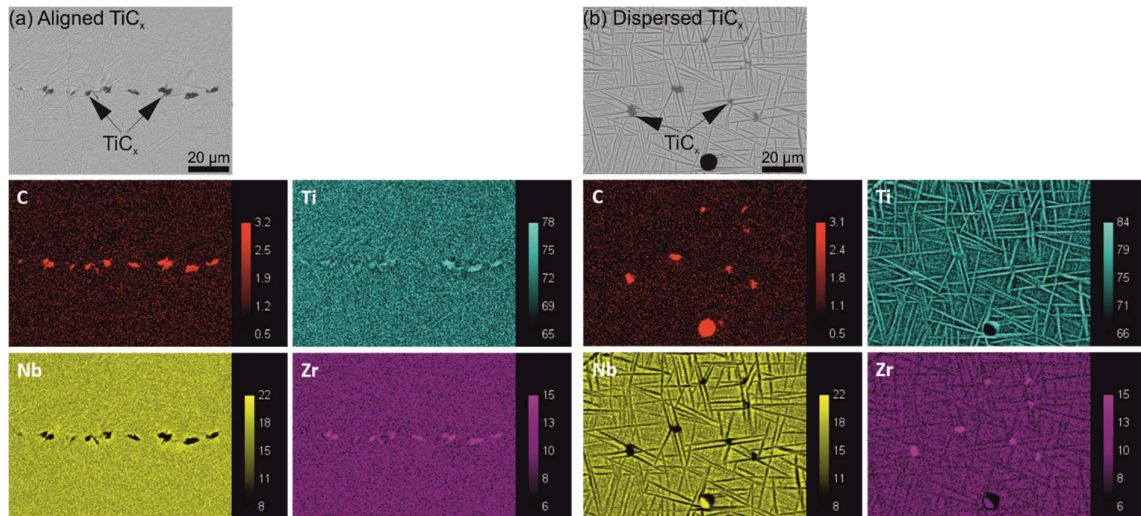
Figure 2 – SEM-BSE images and chemical element mappings of (a) TZN20 with aligned particles; (b) TZN20-Y&CSRA with dispersed particles.
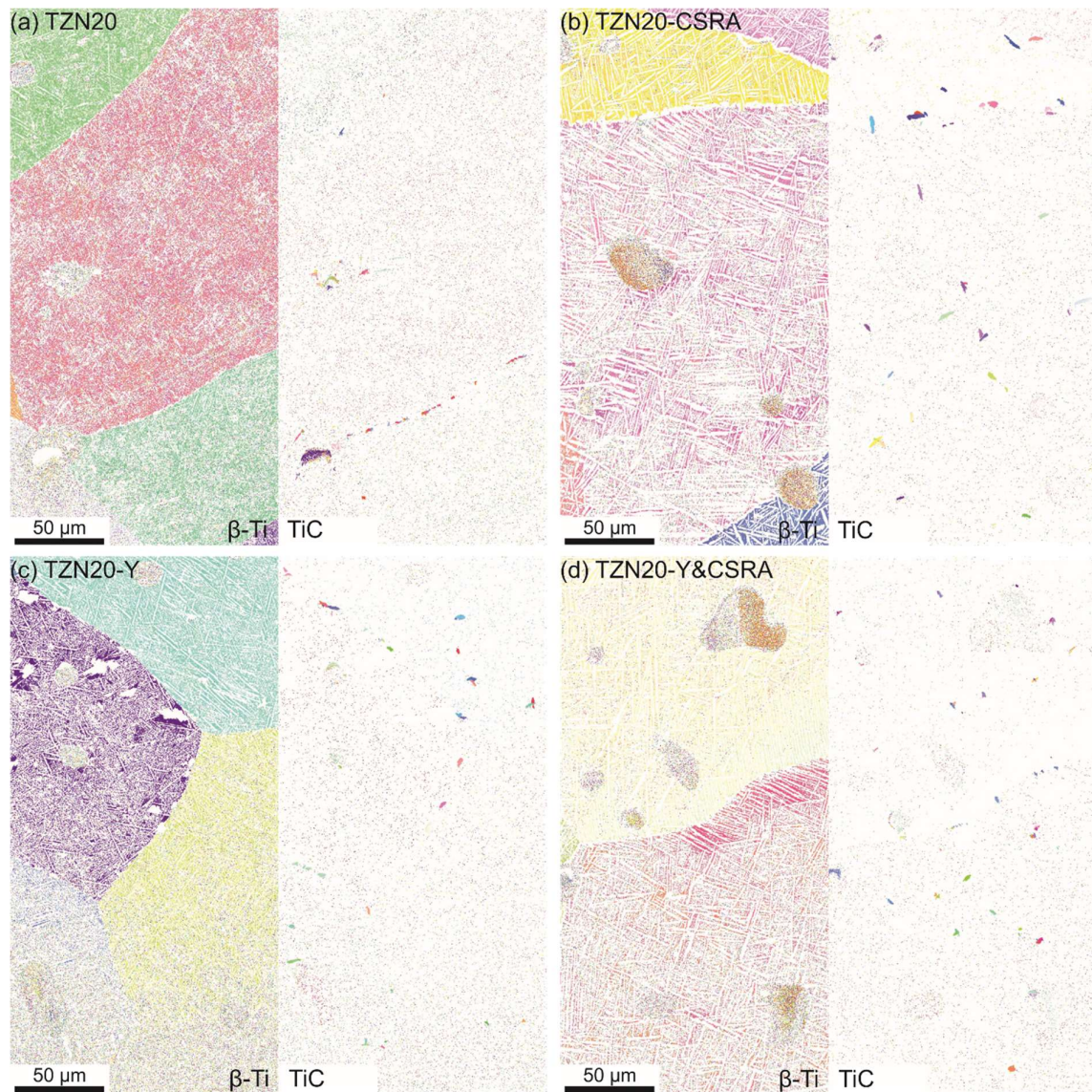
Figure 3:

Figure 3 – Inverse pole figure (IPF) maps of β-Ti phase (left) and TiC phase (right) in (a) TZN20; (b) TZN20-CSRA; (c) TZN20-Y; (d) TZN20-Y&CSRA, in order to identify the precipitating location of TiC_x, i.e. either $GB-TiC_x$ or intragranular TiC_x.

Figure 4:
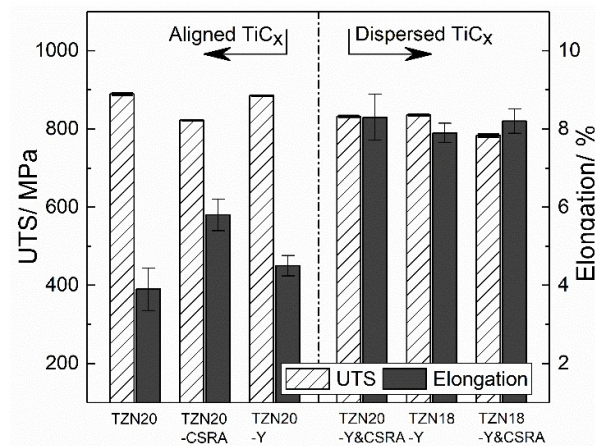
Figure 4 – Ultimate tensile strength (σ_{UTS}) and elongation to fracture (ε_f) of PIM-TZN alloys with different TiC_x particle distributional patterns.

Figure 5:
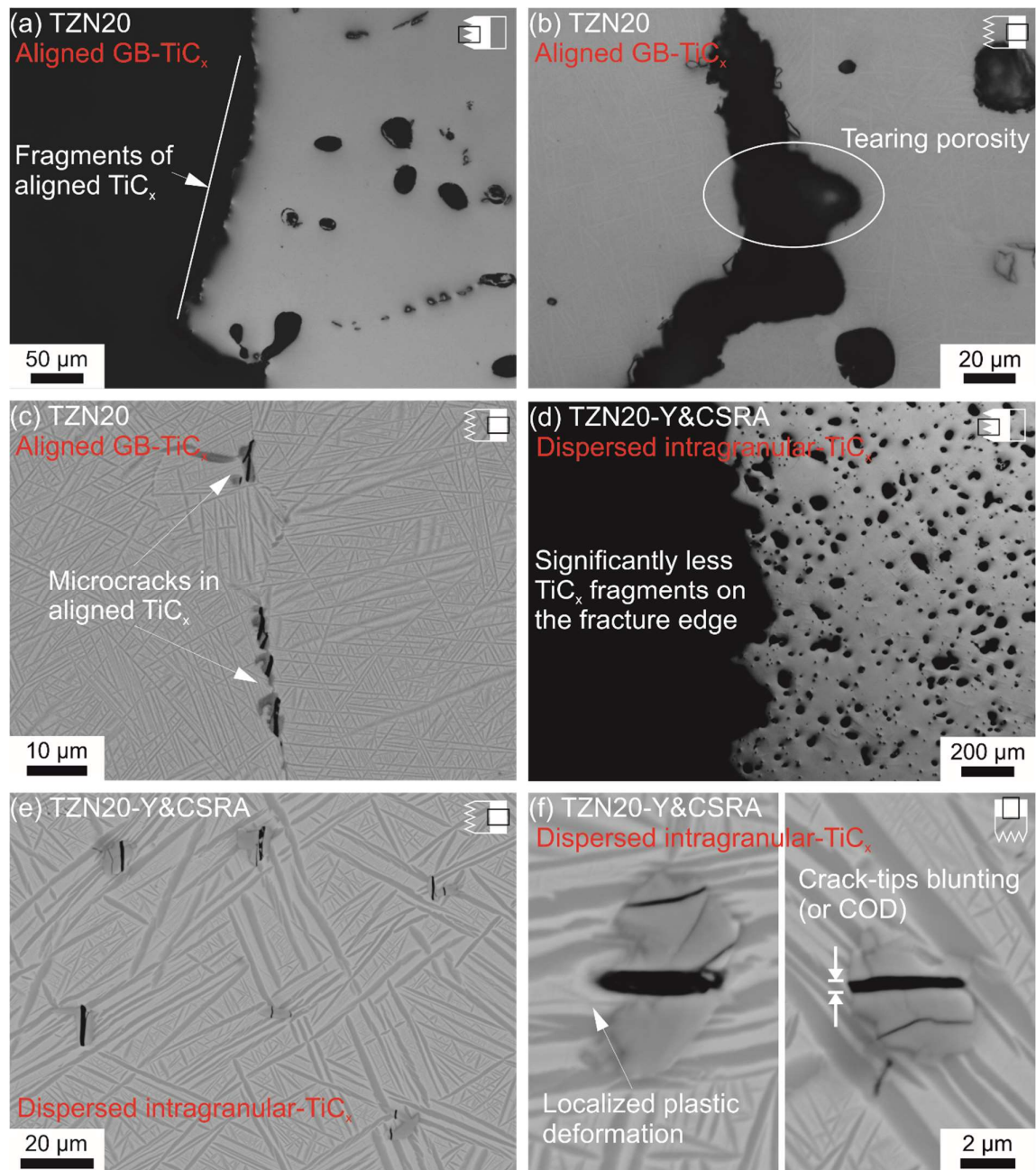
Figure 5 – OM/SEM-BSE fractographic profiles of TZN20 with aligned GB-TiC$_x$ and TZN20-Y&CSRA with dispersed intragranular TiC$_x$: (a) the fragments of TiC$_x$ are in alignment with fracture edge; (b) a typical internal macroscopic crack; (c) aligned microcracks (cracked TiC$_x$) are close; (d) significantly less TiC$_x$ fragments on the winding fracture edge and uniformly

distributed ruptured TiC$_x$ particles in the interior; (e) magnified microcracks initiated in dispersed TiC$_x$ particles, crack tips were frequently pinned at the interface; (f) obvious crack-tips blunting or crack opening displacement (COD) and severe localized plastic deformation suggest a good ductility of the β Ti-matrix.
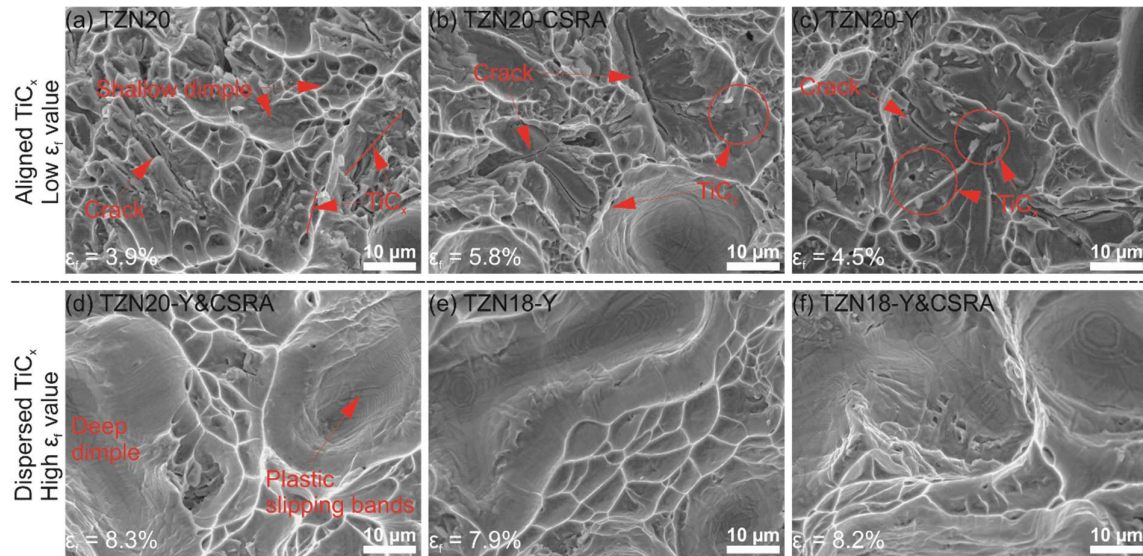
Figure 6:

Figure 6 – SEM-SE images, indicating the implication of TiC_x particles in final fractographs of PIM-TZN alloys. A lot of TiC_x particles or their fragments, large cracks and quasi-cleavage facets were observed in aligned TiC_x cases: (a) TZN20; (b) TZN20-CSRA; (c) TZN20-Y, which suggest TiC_x microcracks coalescence and dislocations cleavage fracture modes occurred. Few TiC_x particles and deeper dimples with apparent plastic deformation slipping bands were found in dispersed TiC_x cases: (d)TZN20-Y&CSRA; the reference group (e) TZN18-Y and (f) TZN18-Y&CSRA, which suggest the crack propagation paths were winding with a number of deflections.
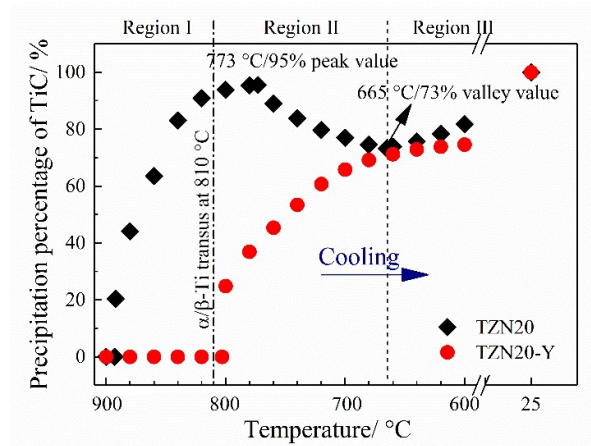
Figure 7:

Figure 7 – The precipitation percentages of TiC$_x$ in relation to the temperature during cooling in PIMed TZN20(-Y) alloys, in order to experimentally model the precipitating evolution of TiC$_x$.
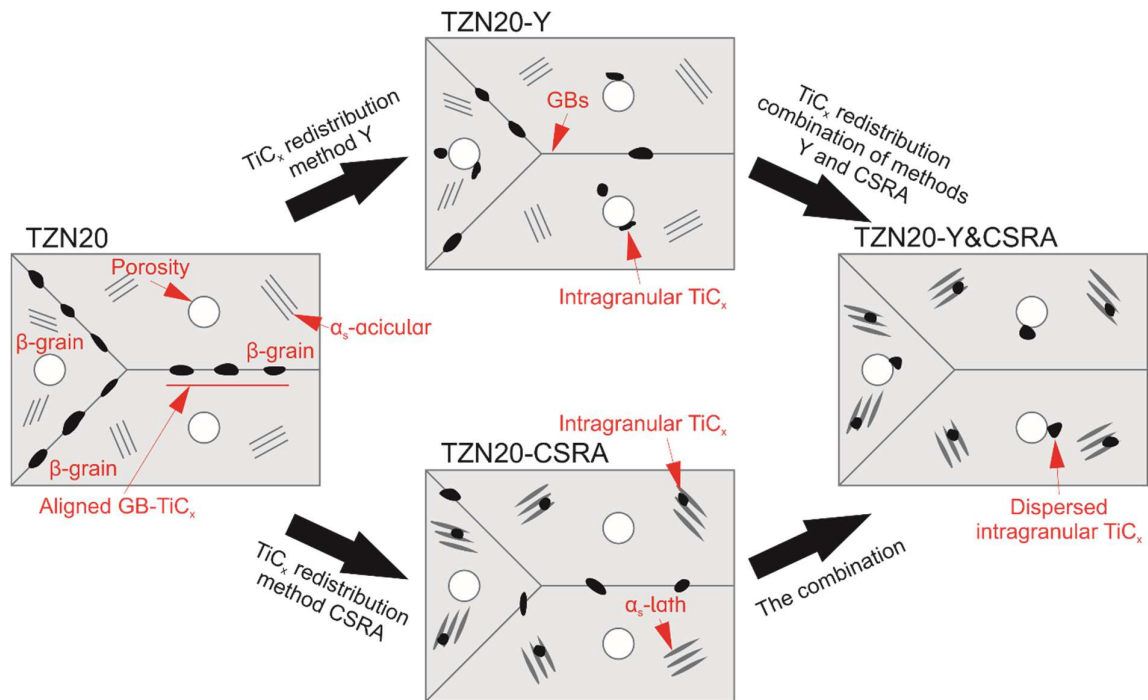
Figure 8:

Figure 8 – Schematic diagram of mechanisms adjusting holistic TiC$_x$ particle distributional patterns by controlling TiC$_x$ precipitating location by using methods of Y, CSRA, and their combination.
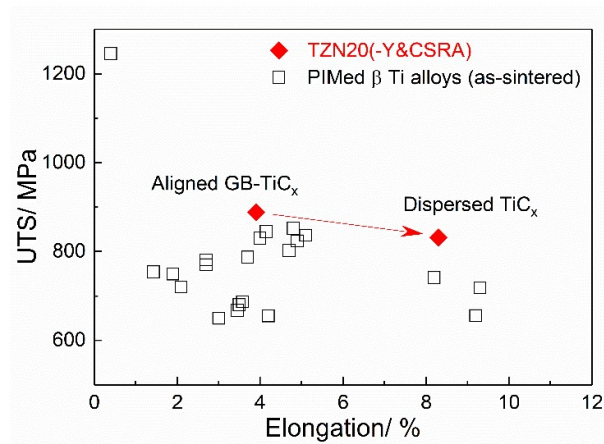
Figure 9:

Figure 9 – Comparison of elongation to fracture (ε_f) and ultimate tensile strength (σ_{UTS}) among representative PIMed β Ti alloys and present PIM-TZN20 alloys with different TiC_x particle distributional patterns.
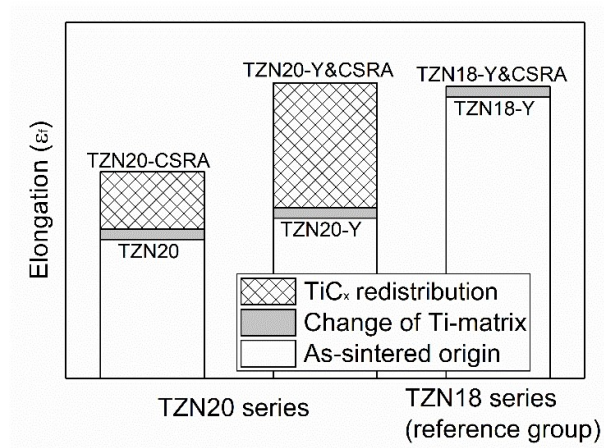
Figure 10:

Figure 10 – Illustration for detailed effects (incl. TiC$_x$ redistribution and the extra) of CSRA on the elongation improvement of PIM-TZN alloys.